JOURNAL OF VIROLOGY, Aug. 2006, p. 7918–7928 Vol. 80, No. 16
0022-538X/06/$08.00+0 doi:10.1128/JVI.00645-06

Supramolecular Architecture of Severe Acute Respiratory Syndrome Coronavirus Revealed by Electron Cryomicroscopy†

Benjamin W. Neuman,[1]* Brian D. Adair,[2] Craig Yoshioka,[2] Joel D. Quispe,[2] Gretchen Orca,[2] Peter Kuhn,[2] Ronald A. Milligan,[2] Mark Yeager,[2,3] and Michael J. Buchmeier[1]

Departments of Molecular and Integrative Neurosciences[1] and Cell Biology,[2] The Scripps Research Institute, 10550 N. Torrey Pines Rd., La Jolla, California 92037, and Scripps Clinic, Department of Cardiovascular Diseases, 10666 N. Torrey Pines Rd., La Jolla, California 92037[3]

Received 30 March 2006/Accepted 30 May 2006

Coronavirus particles are enveloped and pleomorphic and are thus refractory to crystallization and symmetry-assisted reconstruction. A novel methodology of single-particle image analysis was applied to selected virus features to obtain a detailed model of the oligomeric state and spatial relationships among viral structural proteins. Two-dimensional images of the S, M, and N structural proteins of severe acute respiratory syndrome coronavirus and two other coronaviruses were refined to a resolution of ~4 nm. Proteins near the viral membrane were arranged in overlapping lattices surrounding a disordered core. Trimeric glycoprotein spikes were in register with four underlying ribonucleoprotein densities. However, the spikes were dispensable for ribonucleoprotein lattice formation. The ribonucleoprotein particles displayed coiled shapes when released from the viral membrane. Our results contribute to the understanding of the assembly pathway used by coronaviruses and other pleomorphic viruses and provide the first detailed view of coronavirus ultrastructure.

Coronaviruses are an important family of human and veterinary pathogens that can cause enteric and respiratory infections. Coronavirus infection can lead to respiratory failure, gastroenteritis, nephritis, hepatitis, encephalitis, and progressive demyelinating disease (45, 46). Prior to the emergence of severe acute respiratory syndrome coronavirus (SARS-CoV), human coronaviruses were primarily viewed as mundane seasonal pathogens. That perception changed indelibly in 2003 with the epidemic of severe acute respiratory syndrome that emerged from China.

Coronaviruses are classified with the toroviruses, arteriviruses, and roniviruses in the order *Nidovirales*. Nidoviruses share some common aspects of RNA synthesis but diverge in virion morphology. Arteriviruses are spherical and may contain an icosahedral nucleocapsid (81); ronivirus particles are rodlike or pleomorphic (12); torovirus particles are toroidal or pleomorphic (2, 39); and coronaviruses are typically spherical or pleomorphic (16). Coronaviruses derive their name from the protruding oligomers of the spike glycoprotein (S), which form a coronal fringe around the virion. Nucleoprotein molecules (N) and the positive-stranded genome comprise the ribonucleoprotein (RNP) core. The major component of the viral membrane is the triple-pass transmembrane matrix glycoprotein (M), which is essential for virus assembly (reviewed in reference 45).

Coronavirus assembly is localized at membranes of the endoplasmic reticulum-Golgi intermediate compartment (42) and is mediated by species-specific interactions of the M protein with S, N, and envelope (E) proteins. The stringency of structural protein organization at the site of budding is such that some transmembrane host proteins resident at the site of assembly are excluded from the virion, presumably due to tight M-M interactions (18).

Our general understanding of virion organization has been derived primarily from X-ray crystallography and electron microscopic analysis of homogeneous, symmetric viruses, including viruses with helical or icosahedral capsids, and enveloped viruses that display icosahedral symmetry (19, 47). Electron micrographs of coronaviruses show particles that are neither homogeneous nor symmetric (16, 52, 64, 67). Thus, a novel image analysis methodology was applied to overcome some of the limitations posed by pleomorphic particles. Some techniques applied here were originally developed for electron cryomicroscopy (cryo-EM) analysis of pleomorphic arenavirus particles (62) and the envelope of hepatitis B virus (20).

Cryo-EM and image analysis were used to examine the supramolecular structure of three coronaviruses: SARS-CoV, feline coronavirus (FCoV), and murine hepatitis virus (MHV). Single-particle analysis was applied to groups of images collected from similar regions of the virion using iterative alignment and averaging (29). Structural information was extracted from hundreds to thousands of similar partial virion images. Information on vertical organization of viral features was derived from images boxed at the virion edge, designated "edge views," and complementary information on the horizontal distribution and organization of features was derived from "axial views," also known as "en face" views, selected near the virion center. In this report, we present a detailed model of the supramolecular architecture of coronaviruses based on integration of structural data from such axial and edge views.

* Corresponding author. Mailing address: Department of Molecular and Integrative Neuroscience, The Scripps Research Institute, 10550 N. Torrey Pines Rd., La Jolla, CA 92037. Phone: (858) 784-7162. Fax: (858) 784-7369. E-mail: bneuman@scripps.edu.

† This is TSRI manuscript 16733-NP.

TABLE 1. Number of images selected for processing ($\times 10^3$), grouped by virus and orientation

Orientation	Virus			
	SARS-CoV	FCoV	MHV	TUN-MHV
Edge	11.0	5.0	3.0	1.5
Axial	10.0	4.5	2.5	1.5

MATERIALS AND METHODS

Virus growth and purification. Vero-E6, feline AK-D, and murine DBT cells were maintained in Dulbecco's modified Eagle medium (Invitrogen) supplemented with 10% fetal bovine serum (HyClone), 2 mM L-glutamine, and antibiotics. SARS-CoV-Tor2 was propagated on Vero-E6, FCoV-Black was propagated on AK-D, and MHV-OBLV60 was propagated on DBT cells. Viral supernatants were collected 24 h postinoculation, and infectious titers were determined by plaque assay as described previously (63). Virions were harvested from infected cell culture medium by precipitation with 10% polyethylene glycol (PEG-8000). The PEG pellet was resuspended in 0.9% NaCl with 10 mM HEPES and applied to a 10 to 30% sucrose density gradient. Final purification was achieved by ultracentrifugation at 27,500 rpm for 2 h at 5°C. Virus particles resuspended in HEPES-buffered saline were fixed with 10% (SARS-CoV) or 1% (FCoV and MHV) formalin overnight at 4°C prior to cryopreservation.

Cryo-EM. Low-dose cryo-EM was performed at 120 kV as described previously (21). The electron dose was minimized to reduce specimen damage. Digital cryo-EM images were recorded by two methods. SARS-CoV film negatives were digitized using a Zeiss SCAI microdensitometer at a final resolution of 1.84 Å/pixel. All other images were recorded directly via a CCD image sensor at a resolution of 2.26 Å/pixel using Leginon (75). The signal strength and signal-to-noise ratio differed subtly depending on recording methodology. Image contrast was inverted so that protein density appeared white. The density histogram for each image was normalized to a common median gray value prior to analysis.

Image analysis. Image processing was performed using the EMAN (53) and SPIDER (30) software suites. The EMAN module "boxer" was used to manually select regions for analysis (Table 1). Damaged virions were excluded from image selection. The EMAN module "ctfit" was used to estimate the contrast transfer function parameters for each micrograph. At underfocus conditions, the contrast transfer function imposes phase reversals in different spatial frequencies. To eliminate this artifact, particle images were subjected to a low-pass Fourier filter to truncate frequencies beyond the first phase reversal in the contrast transfer function (between 1.6 and 3.5 nm^{-1}).

The x, y origin and rotational orientation of boxed edge and axial views were aligned by 10 rounds of iterative centering and averaging. The EMAN module "startnrclasses" grouped images using factor analysis with k-means grouping to identify covariant features present in particle images. The extracted covariant features were used as a basis for image classification to produce "reference-free" class averages. Particles were classified in groups of 50 to 500 edge views or 100 to 10,000 axial views. Averages for each class were generated by an iterative algorithm, where the average from the previous round was used to align particles for the next average. For each round of alignment, particles that deviated by 1 standard deviation (SD) or more from the mean were excluded from the average for that particular round. About 60% of aligned input images in a group were averaged to produce a final class average.

Radial density profiles. Although the particles were pleomorphic and not circular, 30° sectors within the particles could be identified that had a constant radius of curvature. Radial density profiles for individual sectors were calculated using X3D (9, 10). The bilayer density was used as a fiducial mark for alignment of radial density profiles.

PCA. Axial images were refined by iterative cycles of alignment. Principal component analysis (PCA) was performed to analyze the sources of interimage variation. Principal components (eigenvectors) were extracted from the matrix of aligned axial images using the SPIDER command CA S. The term eigenvector refers to one of a set of ranked factors that describe the prominent covariances found in the input matrix [29]. Each eigenvector was converted to visual form, known as an eigenimage. Eigenimages were reconstituted from the individual eigenvectors using the command CA SRE. The command CA SR was used to reconstitute an approximation of the original axial view images using selected eigenvectors. The relative contribution of each eigenvector to the reconstituted image was weighted in proportion to the prominence of that eigenvector in the original image.

RESULTS

Ultrastructure of frozen hydrated coronavirus particles. Cryo-EM images of coronavirus particles showed fields of enveloped, spherical, and ellipsoidal virions (Fig. 1 and 2). A fringe of cone-shaped spikes protruded from the viral envelope. The virion core contained ~5-nm punctate densities. Particle diameters ranged from 50 to 150 nm, excluding the spikes, with mean particle diameters of 82 to 94 nm.

The precision of other measurements was assessed by measuring the distance between the inner and outer bilayer headgroup densities from empty vesicles that were copurified with virions. Bilayer headgroup densities were separated by 3.8 nm with a standard error of ±0.1 nm (0.5 pixel) and an SD of ±0.5 nm, or 2.5 pixels ($n = 45$). Published studies indicate that the electron-dense phospholipid headgroup regions within bilayers are separated by 3.6 to 4.0 nm in most common cellular lipid membranes (58). Thus, from the coronavirus bilayer measurement, it was determined that densities in these images could be measured with subnanometer accuracy and precision.

Characterization of viral spikes. Spikes extended ~19 nm (SARS-CoV and MHV) to 21 nm (FCoV) from the high-density headgroup region of the outer bilayer leaflet. Tunicamycin (TUN) treatment induces misfolding of the spike protein (S) and leads to the formation of spike-depleted virions (68, 69). TUN-MHV therefore served as a spike-depleted control. Spike-depleted TUN-MHV (Fig. 1E) and TUN-SARS-CoV particles (not shown) displayed otherwise normal "coronavirus-like" morphology. The mean diameters of TUN-grown and native MHV particles did not differ significantly (TUN-MHV [means ± SD], 93 ± 17 nm [$n = 87$]; MHV, 89 ± 13 nm [$n = 80$]; $P > 0.05$ by t test). Thus, the surface spike is dispensable for formation of authentic virus-like particles, as previously reported (11, 34, 38, 80).

Characterization of proteins M and N. The appearance of closely packed densities in the membrane and the punctate electron-dense features in the core of all three coronaviruses supported attribution to the remaining, conserved, high-copy structural proteins M and N, respectively. M is known to be membrane embedded, and the carboxyl tail interacts specifically with N (26, 43, 59, 74). The M-N interaction should therefore constrain some N molecules in close apposition to the envelope. To characterize the M-N interaction, density was plotted as a function of radial distance relative to the viral membrane. Fewer than 1% of the imaged virions were found to be sufficiently circular to permit successful whole-particle radial density analysis. However, analysis of the density within 30° virion sectors yielded more consistent results. Two high-density features were consistently detected on the inner bilayer leaflet of virion images (Fig. 3A). The 1-nm layer of density directly apposed to the inner bilayer headgroup was ascribed to M. The second feature, centered 12 nm below the inner headgroup density, was ascribed to N in the form of the viral RNP. The centers of mass for interacting M and N molecules were therefore separated by ~10 nm.

Analysis of structural protein spacing. The Fourier transformation is a mathematical operation that resolves a signal into amplitude and phase components as a function of frequency (for a review of single-particle EM techniques, including Fourier transformation, see reference 29). Fourier trans-

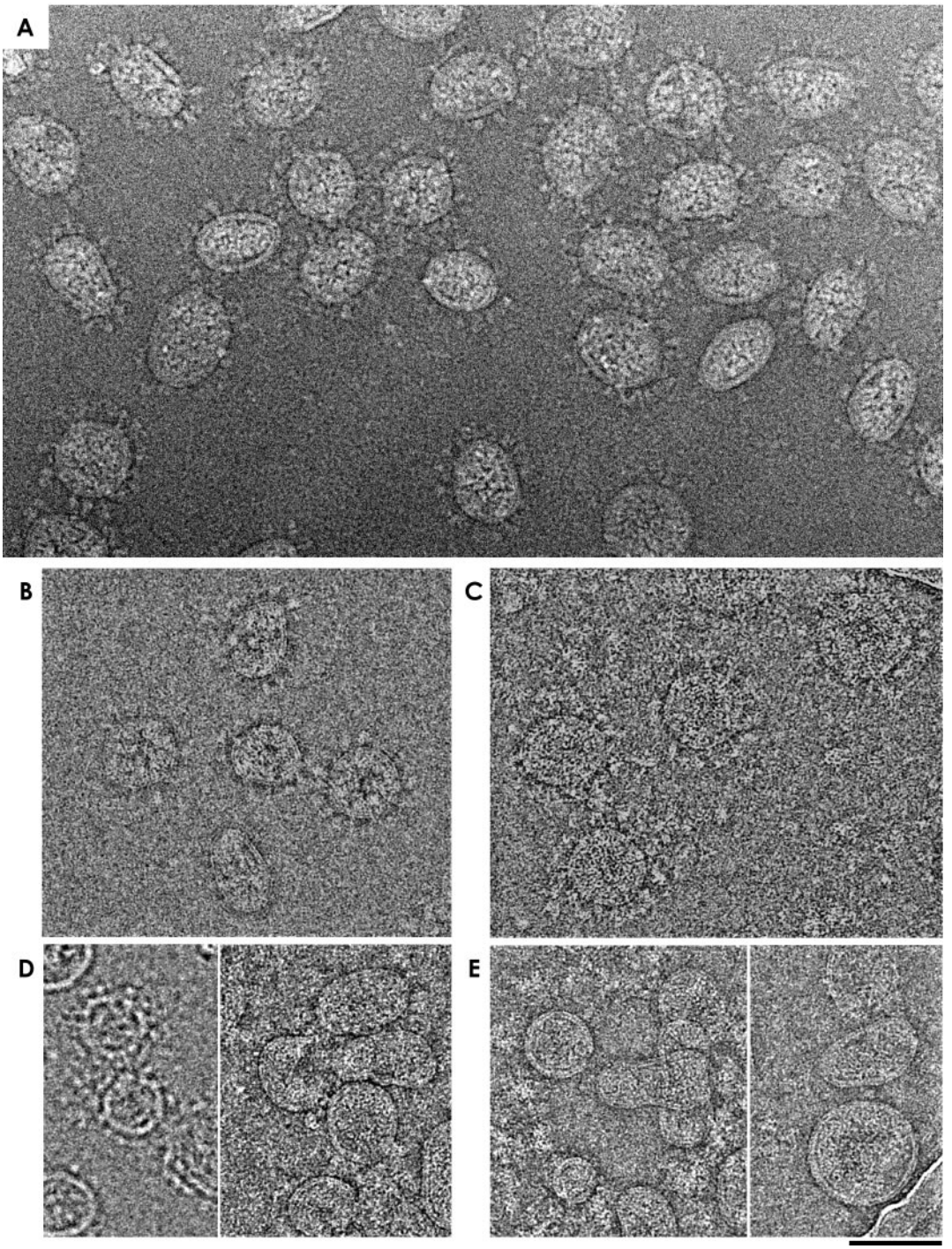

FIG. 1. Cryo-EM of coronaviruses in vitreous ice. SARS-CoV-Tor2 (A and B), FCoV-Black (C), MHV-OBLV60 (D), and tunicamycin-grown MHV-OBLV60 (E) are shown in "reversed" contrast, with density in white. Images were recorded at ~2.5 microns below true focus (B, C, right-hand portion of panel D, and E), ~4.0 microns under focus (A), and ~20 microns under focus (left-hand portion of panel D). The scale bar represents 100 nm.

formation can be used to analyze the size and spacing of component features within a two-dimensional image, such as an electron micrograph. Periodicity within an image will produce peaks in the power spectrum, a plot of the amplitudes of the Fourier transform versus spatial frequency. Power spectra were calculated from images of coronavirus particles that were recorded at several focus levels; results from two focus levels are shown in Fig. 3B. Adjacent regions of background vitrified ice were analyzed for each specimen as controls. The power spectra of ice-embedded virions displayed two prominent peaks of intensity, which were absent in the power spectra from images of the background vitrified ice. A sharp peak at 15

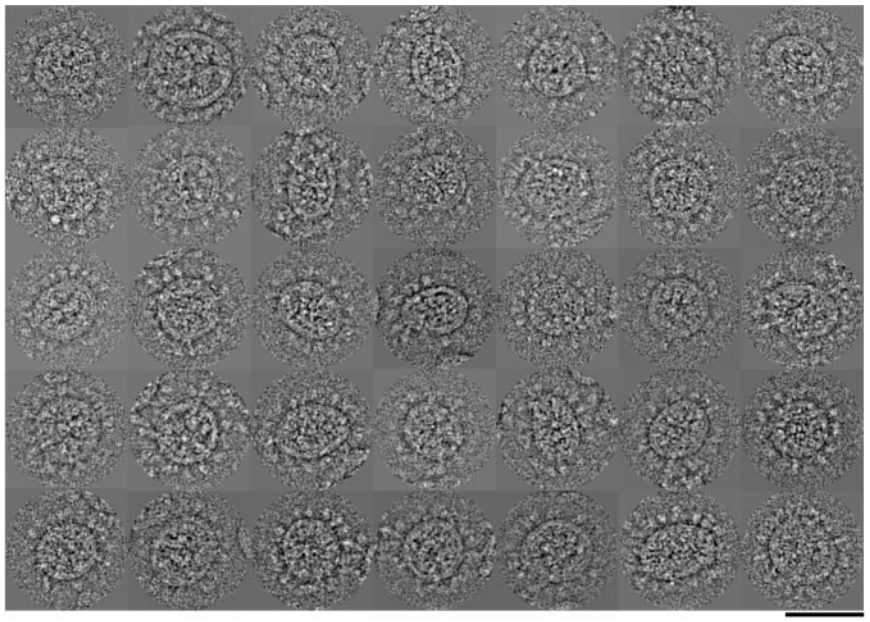

FIG. 2. Cryo-EM of pleomorphic SARS-CoV virions. Shown is a gallery of images at −2 to −4 microns defocus to illustrate surface and interior topography. The scale bar represents 100 nm.

nm^{-1} and a broader peak at 5 to 8 nm^{-1} were observed for SARS-CoV (Fig. 3B). Power spectra from images containing MHV and FCoV particles displayed similar features (data not shown).

The 15-nm^{-1} and 5- to 8-nm^{-1} features were also present in power spectra of boxed regions of virion images, including axial views (data not shown) and edge views (Fig. 3C). The physical separation of S, M, and the RNP in edge views affords an opportunity to dissect the origins of prominent peaks in the power spectra. SARS-CoV edge views with central spikes were aligned so that the membrane was horizontal. Each image was then divided into an "inner" half containing the RNP and an "outer" half containing spikes (Fig. 3C, inset). Power spectra of spike-depleted TUN-MHV particles lacked the 15-nm^{-1} feature present in native SARS-CoV edge views, which confirmed the assignment of this peak to the spikes (data not shown). The 5- to 8-nm^{-1} peak was not related to the spikes and instead originated primarily from the RNP. Dissection of FCoV and MHV edge views yielded the same attribution of densities (data not shown).

The 15-nm^{-1} peak did not match measurements of the spike height (~19 to 21 nm) or width (~10 nm). Therefore, interspike spacing was investigated as a possible source of the 15-nm^{-1} peak in the power spectra. To accomplish this, aligned edge views were duplicated and divided into outer, middle, and inner thirds, containing spikes, membrane, and RNP, respectively (Fig. 3C, inset). One copy of each image was shifted horizontally in 1-pixel increments and compared to the second, static copy, with the results expressed as a correlation coefficient. Correlation coefficients are expressed on a scale of −1 to 1, with positive values indicating positive correlation. Correlation peaks at 13 to 15 nm in the outer and middle regions reflected the most commonly observed interspike spacing (Fig. 3D). A small increase in correlation between 5 and 8 nm in the RNP region was insufficient to characterize the inter-RNP spacing.

Lattices of spike and RNP densities. Analysis of the edge views revealed that the 15-nm^{-1} spike and 5- to 8-nm^{-1} RNP features in the power spectra were not interdependent, so they could be analyzed separately (Fig. 3C and D). Analysis of axial views of spike-depleted and native coronavirus particles provided an independent approach for examining the structure of the envelope without any assumptions regarding the symmetry or packing of the glycoprotein surface spikes. By extracting areas in the center of the particle, the radius of curvature is sufficiently small that, at least at low resolution, we can treat these areas as if they were planar. Axial images represent the superposition of the near and far sides of the virus as well as any interior density. The process of reference-free alignment was presumed to favor the less distorted or more prominent side of the virion, although we were not able to test this assumption directly. Fourier space filtration was therefore applied to resolve the spike and RNP contributions in axial views, where the two features overlap (Fig. 4). Axial images were filtered to remove image components either larger or smaller than 9 nm. Filtered images were then iteratively aligned and averaged in real space. Images of background ice were processed similarly to control for artifacts that might have been introduced during the filtration process. Features larger than 9 nm were refined as round, 10-nm-diameter spikes. The spike spacing approximated an oblique planar crystallographic lattice with a unit cell with edges of ~14 and 15 nm and an angle of ~100° (Fig. 4C, row c). Analysis of axial images of spike-depleted TUN-MHV showed no lattice, confirming the assignment to the glycoprotein spikes (Fig. 4C, column 4, row c).

Features smaller than 9 nm in SARS-CoV, FCoV, MHV, and TUN-MHV axial images were refined as arrays of oval

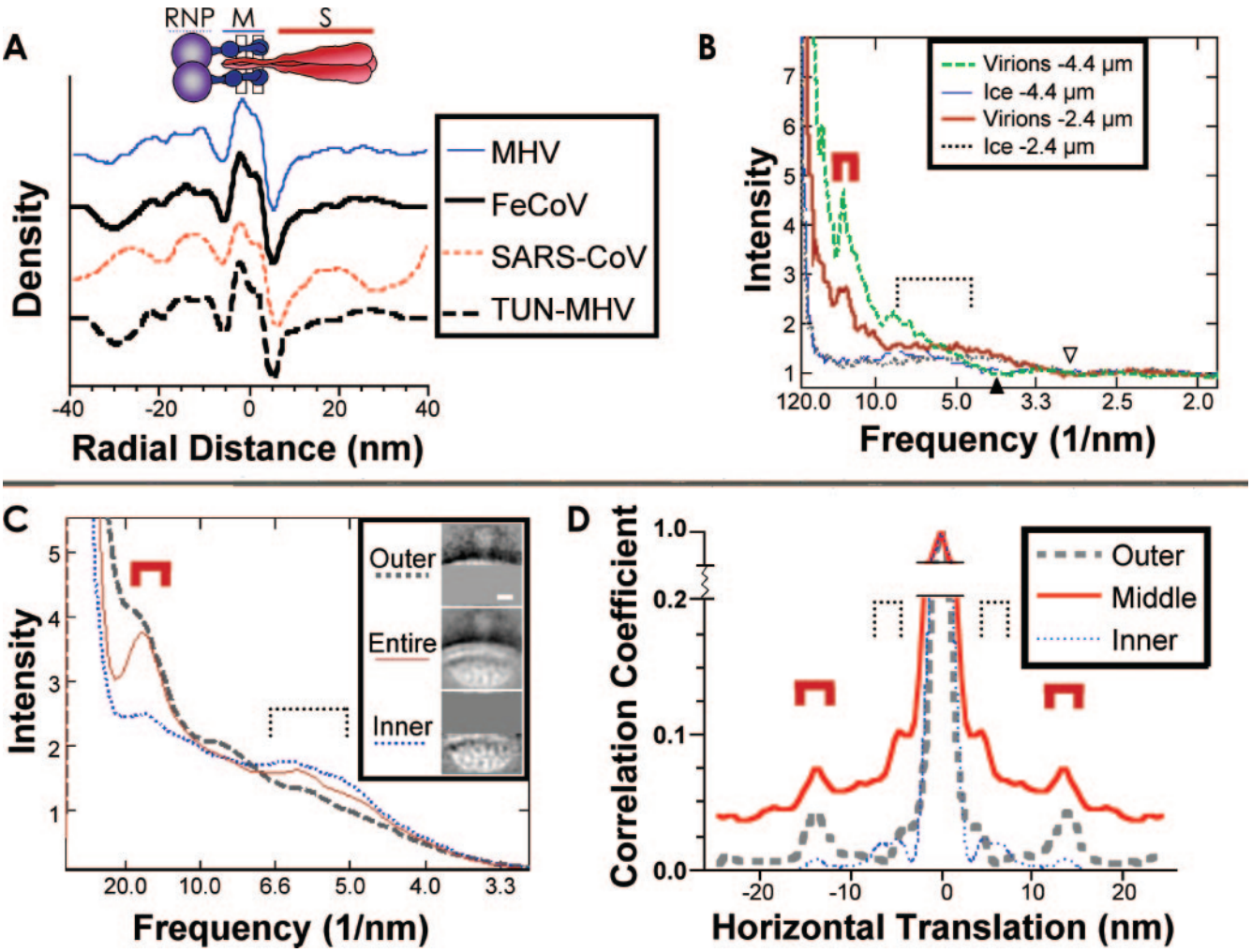

FIG. 3. Disposition of densities in the membrane-proximal region. (A) Rotationally averaged radial density profiles were generated for 30° wedges taken from intact coronavirus particles. Wedges from SARS-CoV (n = 80), FCoV (n = 41), MHV (n = 53), and TUN-MHV (n = 82) particles were aligned on the minimum-density node between the headgroup densities of the lipid bilayer. The schematic above interprets densities in the spike protein (S), membrane-proximal and matrix protein (M), and ribonucleoprotein (RNP) regions. Entire SARS-CoV virions and adjacent regions of background vitrified ice, recorded at two levels of focus, are presented as reciprocal space power spectra (B). Prominent features are noted at ~15 nm^{-1} (heavy red bracket) and ~5 to 8 nm^{-1} (dotted bracket). An averaged power spectrum for ~1,000 aligned SARS-CoV edge views (C) or the extraviral (outer) or interior (inner) portion of the image is also shown. The scale bar represents 10 nm. Prominent features are marked as described for panel B. Edge views (C, entire) were divided into upper (D, outer), membrane-proximal (D, middle), or lower (D, inner) thirds. The correlation coefficient was calculated for a static copy of each image and another copy of the same image that was shifted in 1-pixel increments. Peaks of correlation are marked as described for panel B.

RNP densities. RNP densities of 5 by 6 nm were arranged in an ~100° oblique lattice, with unit cell edges of 6 and 7.5 nm (Fig. 4C, row a). Fourier transformation of the spike and RNP lattices yielded first-order reflections (insets), consistent with locally ordered planar packing. Similar reflections also originated from the centers of some individual particles (Fig. 4D). The 6.0- to 7.5-nm inter-RNP reflections imply medium-range "paracrystalline" packing, with consistent spacing but variable alignment of fine features. The RNP densities were consistent with the dimensions and appearance of coronavirus RNP released from disrupted virions (15, 55).

We then analyzed the superposition of lattices of the spike and RNP features. Reflections from Fourier-transformed class averages of axial views were isolated and used to reconstruct the spike and RNP lattices. Reconstructed SARS-CoV, FCoV, and MHV spikes and RNP lattices were found to be nearly identical. Each spike was positioned centrally over four RNP densities (Fig. 5).

The resolution limit of the axial class average images was next examined. Class averages were refined using only the even- or odd-numbered images in a class and then compared by Fourier ring correlation (FRC) analysis (71). The point where the FRC value equaled 0.5 was taken as the nominal resolution limit. Arrays of RNP densities in axial class averages were resolved to 5.3 to 5.8 nm (Fig. 4C and D and 5A).

Oligomerization of S. Principal component analysis (PCA) is a statistical technique that can be used to examine interimage variance. Here, PCA was applied to improve the resolution of spikes in the axial images. Coronavirus spikes have been reported to be homotrimeric based on structures of the fusion-

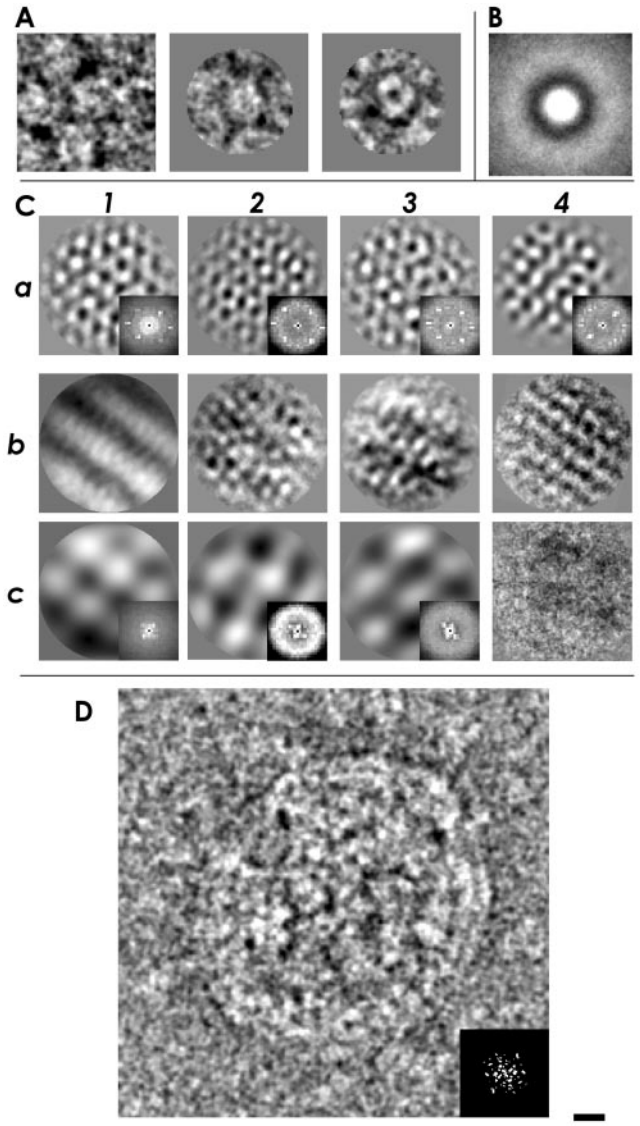

FIG. 4. Analysis of viral features in axial views. (A) Axial spike images were selected from the central region of each virion (left image) and masked around one spike (center and right images). (B) An averaged image from unaligned, unmasked, manually centered SARS-CoV axial views is also shown. (C) Axial images of SARS-CoV (column 1), FCoV (column 2), MHV (column 3), and TUN-MHV (column 4) were aligned and averaged iteratively until a stable averaged image emerged (row b). Axial images were filtered in Fourier space to remove image data greater than (row a) or less than (row c) 9 nm. Filtered axial images were averaged, the averaged image was refined by 10 rounds of iterative alignment and averaging, and then unfiltered images were aligned to the averaged filtered image for a further two cycles to produce the images shown (rows a and c). Insets show Fourier transforms of the corresponding averaged images. (D) One virion that displayed reflections corresponding to the spike and RNP lattices is shown, together with a Fourier transform of the core region (inset). The scale bar represents 10 nm.

activated core (24, 76, 79, 85, 86). However, some reports have described homodimeric forms of the spike (7, 48).

Some reference-free class averages of axial views appeared to show triangular spikes (Fig. 5E, left). To investigate further, a SARS-CoV reference-free class average was refined using ~1,000 axial images. Principal components (eigenvectors) were extracted from the matrix of aligned images.

Prominent eigenimages showed ~10-nm-diameter spikes, situated ~15 nm apart (one example is presented in Fig. 5E, center). Individual axial-view images were reconstructed from the weighted contributions of four prominent eigenvectors showing spikes. Three-lobed spike densities were reconstructed from axial SARS-CoV images (Fig. 5E, right). Intralobe spacing within the trimer was ~6 nm. Reconstructed FCoV and MHV spikes also showed similar three-lobed densities (data not shown).

Images of ice and axial TUN-MHV images were analyzed by PCA as a control. Eigenimages from background ice resembled featureless noise. Axial TUN-MHV eigenimages and reconstructed images showed only the RNP lattice (Fig. 5F). The observed three-lobed densities therefore originated only from images showing spikes.

The approximate volume occupied by a spike was estimated as another way to assess the oligomeric state of the S protein in the spikes. The average partial specific volume of folded protein, measured at ~0.73 cm^3/g (36), was used to calculate the expected volume of the spike ectodomain. One copy of a SARS-CoV (130 kDa), FCoV (151 kDa), or MHV (137 kDa) S protein ectodomain was therefore predicted to occupy 1.8×10^2 to 2.1×10^2 nm^3, for a hypothetical volume of 5.4×10^2 to 6.3×10^2 nm^3 per trimer. Axial and edge projections of the spike were measured from class averages and images that had been filtered to remove high-resolution noise. On the basis of the dimensions of the spikes, the volume of an ellipsoidal spike "head" on a cylindrical "stalk" was estimated at 4.9×10^2 to 5.9×10^2 nm^3. Spikes that were modeled instead as cone segments gave estimated volumes of 5.2×10^2 to 5.8×10^2 nm^3. The volume of each spike ectodomain is therefore consistent with a homotrimer.

Estimation of S:N stoichiometry. The volume of the RNP densities was next estimated. RNP densities modeled as ellipsoids gave estimated volumes of 53 to 73 nm^3. The predicted protein volume for the N monomer of SARS-CoV, FCoV, or MHV is 51 to 60 nm^3 (36). Each RNP density therefore contains one N protein molecule. The native coronavirus spike was thus found to be trimeric and was situated over four RNP densities, each likely consisting of one nucleoprotein density plus RNA. The ratio of S to N at the virion surface was therefore found to be three copies of S to four RNP densities (S_3:4N). The observed structural unit of $1 \times S_3$:4N is also consistent with the dimensions of the spike and RNP unit cells.

Vertical organization of the S-M-RNP complex. Edge view images were refined to examine the stoichiometry of S:M and M:N. M is present in higher copy numbers than N or S in the virion (6, 25, 35), and it likely plays a pivotal role in assembly. Well-defined edge-view class averages were obtained by masking out parts of the images that showed the highest variability. Empirical testing revealed that a keystone-shaped mask (Fig. 6A and B) incorporating one spike and two adjacent RNP densities of the membrane-proximal shell (Fig. 6C) gave the optimal results. The area refined most clearly corresponded to a side projection of the unit cell that was identified in axial views.

Refined FCoV edge views (Fig. 6D) showed spikes with elongated stalk regions that may correspond to the extended

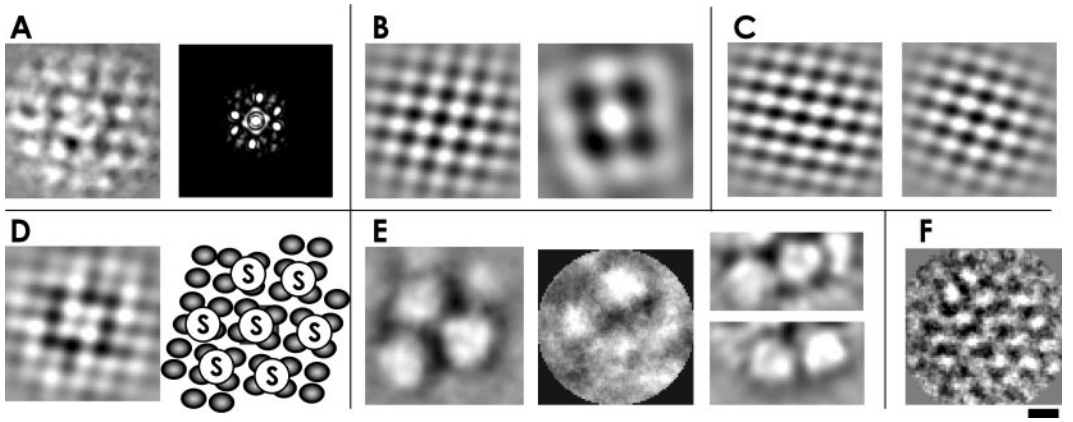

FIG. 5. Analysis of SARS-CoV paracrystalline lattices. The SARS-CoV RNP lattice (Fig. 4C, column 1, row a) was used as the starting image for 10 cycles of alignment and averaging (A, left image). Reflections were selected from the Fourier transform of this image (A, right) and back transformed to reveal the overlapping RNP (B, left) and spike (B, right) lattices. (C) Lattices similarly obtained from reflections in Fourier transformed FCoV (left) and MHV images (right) show similar RNP organization. (D) The two lattices are shown superimposed and averaged (left) and in schematic form (right). (E) A reference-free class average of axial SARS-CoV images recorded slightly farther from focus shows triangular spikes (left), also seen in the example principal component eigenimage (center) and in reconstructed images (right). (F) An example eigenimage from TUN-MHV, showing only RNP densities, is presented for comparison. The scale bar represents 10 nm.

amphipathic heptad-repeat regions predicted to reside within the stalk region (4). Refined edge views of TUN-MHV particles showed multiple RNP densities with no external spikes (Fig. 6F). Spikes were resolved most clearly in images with only one layer of resolved RNP densities (Fig. 6C to E). Analysis of interimage variability confirmed that the spikes are in register with only the RNP densities in the outermost shell and that regions outside the aligned densities are highly variable (data not shown).

The resolution of edge-view class averages was measured by FRC analysis as described for the axial views. The nominal resolution of the SARS-CoV and FCoV edge class averages was 4.2 to 4.7 nm. TUN-MHV edge-view class averages were resolved to 3.8 to 4.3 nm. MHV edge-view class averages were more poorly resolved (>6 nm), likely due to glycoprotein shedding during purification.

Characterization of M. Intramembrane densities were poorly resolved in class averages. However, intramembrane densities spaced 3 to 5 nm apart were observed in some raw virion images (Fig. 6G and H). Similar intramembrane densities were observed in spike-depleted TUN-MHV. M is known to be a triple-pass integral membrane protein (18). Therefore, the intramembrane densities were related to transmembrane regions of M rather than S. Densities spaced 5 to 8 nm apart connected the RNP to the membrane region (Fig. 6G and H, white arrowheads), consistent with the spacing of paracrystalline RNP. The 5- to 8-nm connecting densities could not be ascribed confidently to M or N.

Spherical and coiled RNP configurations. Edge views revealed that most of the viral RNP was located within ~25 nm of the inner face of the membrane (Fig. 6A). The diameter of coronavirus RNP complexes released from disrupted particles has been reported to be 14 to 16 nm (15, 55). Fifteen-nanometer-wide strands of electron-dense material can be seen emerging from a spontaneously disrupted SARS-CoV particle (Fig. 6I). The appearance of the 15-nm strands is consistent with published descriptions of helical-form coronavirus RNP (15, 55). The RNP is maintained in a spherically packaged form at the inner face of the membrane (Fig. 6I, large and small black arrowheads). Flat-edged cores, three- and fivefold symmetry axes, and other hallmarks of icosahedral symmetry were not detected in the images of frozen-hydrated coronavirus particles. These results did not rule out the possibility that local paracrystalline ordering could give rise to the cores with some planar surfaces reported by others (67).

DISCUSSION

In this study, cryo-EM and image analysis were used to examine the structure of three coronaviruses: SARS-CoV, FCoV, and MHV. Our results demonstrate a higher level of supramolecular organization in the viral envelope region than was evident from previous EM studies, and they therefore suggest some modifications to previous interpretations of coronavirus structure (23, 54, 73), as shown in Fig. 7. Glycoprotein spikes were found to be aligned with the membrane-proximal layer of RNP densities, implying that protein location within the envelope is constrained by consistent S-M, M-M, and M-N interactions. The clustering of viral features near the membrane was consistent with published biochemical data showing S-M (17, 34), M-M (18), and M-N (26, 43, 59, 74) interactions. Although some particles displayed membrane densities ascribable to M (Fig. 6G and H), the relative visualization of M in cryo-EM images of whole virions may have been limited by the signal-to-noise ratio (Fig. 3B). Visualization of M would also be obscured by the large signal arising from the phospholipid headgroups of the viral membrane in edge views. However, M interacts with both S and N. Results presented here confirm the observation of Risco and collaborators (67) that the coronavirus nucleocapsid is separated from the envelope by a gap, which we have revealed to contain thread-like densities that connect the M protein density on the inner face of the viral membrane to a two-dimensionally ordered ribonucleoprotein layer (Fig. 6G and H). Organization of S and N in related

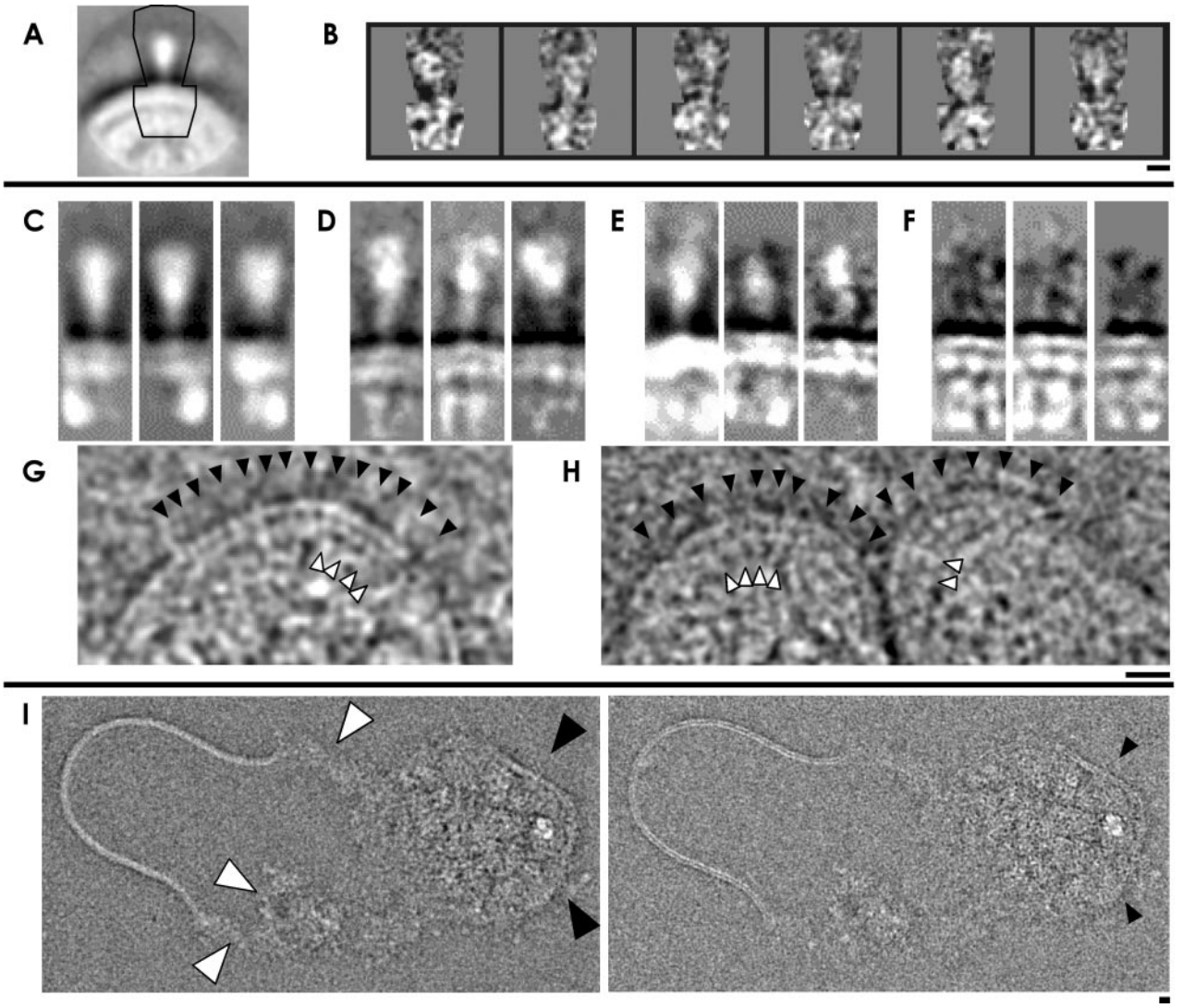

FIG. 6. Analysis of the structural proteins as seen in edge views. (A) Boxed images were centered on the viral membrane below one spike, as shown in the averaged image of aligned SARS-CoV edge views. (B) A keystone-shaped mask (shown in panel A) was applied to individual edge views before reference-free classification and averaging. (C) Edge-view class averages show the ultrastructure of the membrane-associated structural protein complex. Class averages of FCoV (D), MHV (E), and spike-depleted TUN-MHV (F) were obtained by the same process. Intramembrane densities ascribed to viral M protein are indicated with black arrowheads in SARS-CoV (G) and TUN-MHV (H). Connecting densities between the RNP and membrane regions are indicated with small white arrowheads. (I) A spontaneously disrupted SARS-CoV particle shows RNP strands escaping from a spherical core, recorded at −4 μm (left) and −2.4 μm (right) under focus. The narrowest parts of the RNP are indicated with white arrowheads, and the membrane section remaining with the core is indicated with large black arrowheads (left). The bilayer densities are more visible in the near-focus image, indicated with small black arrowheads (right). The scale bars represent 10 nm.

lattices implies that M is also organized in a two-dimensional lattice, and it may provide a scaffold for viral assembly. M contains three transmembrane helices (18). The observed ~2-nm-wide intramembrane M densities could accommodate a bundle containing the three ~1-nm transmembrane helices originating from one M protein molecule. However, further investigation will be needed to determine the structural basis for the inferred M protein scaffold. On the basis of our current analysis, we estimate the stoichiometry of the unit cell at the virion surface to be approximately $1S_3$:16M:4N to $1S_3$:25M:4N proteins, with the remainder of the N protein distributed throughout the virion core.

The presence of overlapping scaffolds of viral proteins in the envelope is likely related to the mechanism of viral budding, but this does not specifically explain the formation of closed spherical virions. Particle closure would require some mechanism of disrupting the two-dimensionally ordered S:M:N scaffold. Our analysis did not reveal any consistent structural perturbations that could explain the mechanism of particle closure. The single-particle analysis methods applied in this study rely on averaging to determine the most common arrangement of proteins. As such, these methods are well suited to analysis of the "guiding principles" of coronavirus particle formation but are poorly suited to the analysis of structural microheterogeneity. A possible mechanism by which minor membrane constituents, such as E and the group-specific inte-

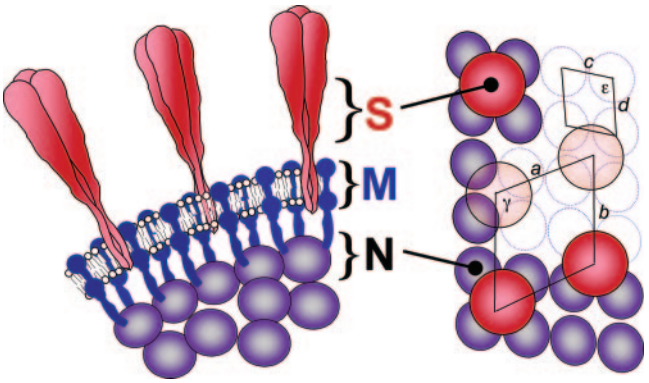

FIG. 7. Interpretation of coronavirus virion structure. Conserved structural proteins are drawn as they appear in edge views (left) and axial views (right). Trimeric spikes (S) are shaded in red, membrane proteins (M) are in solid blue, and nucleoproteins (N) are shaded in violet. The dimensions of lattices of S trimers (a = 14.0 nm, b = 15.0 nm, γ = 100°) and RNP molecules (c = 6.0 nm, d = 7.5 nm, ε = 100°) were determined from the reflections shown in Fig. 5A and were consistent with real-space measurements of the same parameters.

gral membrane structural proteins, may promote membrane curvature is implied by data indicating that mutations in E result in a higher proportion of aberrantly budded virions (27). Expression of SARS-CoV E was recently shown to induce membrane permeabilization (51), and other coronavirus E proteins induce the formation of convoluted membranous structures similar to those seen in coronavirus-infected cells (14, 65). We therefore hypothesize that E might disrupt sheets of paracrystalline S, M, and N by intercalating among M proteins during assembly. MHV lacking E is viable, although highly attenuated (44), suggesting that the role of E in virogenesis is either dispensable or that the role of E during budding can be compensated by other viral and cellular proteins. SARS-CoV particles likely contain at least the three-pass integral membrane protein Sars-3a (78, 83) and the type I transmembrane protein Sars-7a (78), in addition to the E protein homolog encoded by subgenomic RNA 4. Further investigation will be required to determine how the E protein and the other coronavirus group-specific proteins contribute to particle formation.

A coronavirus particle of average diameter with a full complement of spikes could contain ~50 to 100 spike trimers and ~200 to 400 copies of N in the membrane-proximal lattice region, depending on whether the spike or RNP spacing is used to calculate the surface area of a spike unit cell. The ratio of S:N in surface lattices may decrease if some particles bud with less than the full complement of spikes, as in the case of TUN treatment. The observation of an oblique lattice of trimeric spikes at the virion surface was unprecedented. Simple hexagonal close packing of homotrimeric S should define a 120° unit cell with a lattice spacing reflecting the 10-nm spike diameter. Retroviral particles, for example, appear to contain hexagonally arranged proteins (32, 61, 88). Placement of coronavirus spikes is therefore likely controlled by interaction with other ordered components of the virion. S is captured at the site of budding by the presence of M; thus, interaction with M is a likely source of S organization. Nucleoprotein molecules in the paracrystalline RNP shell abut, and may be partially organized through, interactions at points of contact in the RNP lattice (Fig. 5B and C). The distribution of density in the viral core was consistent with a membrane-proximal RNP lattice formed by local approaches of the coiled ribonucleoprotein. Dimeric N-N interactions (8, 37, 49, 77) are another possible source of virion organization. For instance, it was recently observed that the N protein dimerization domains of arteriviruses and coronaviruses share a common fold despite low homology (8). Further experimentation will be required to determine how N-N interactions contribute to arterivirus core morphology.

Emerging evidence suggests that membrane-proximal protein lattices may be characteristic of enveloped non-icosahedral viruses and may represent an alternative to icosahedral and helical symmetry in virion architecture. For example, cryo-EM and cryoelectron tomography have demonstrated that glycoprotein spikes in the poxvirus core envelope (13, 22) and the envelope of hepatitis B virus (20) are hexagonally packed. Retroviral Env may be organized similarly: hexagonal arrays were described for human foamy virus (82), and loose hexagonal packing was noted for human immunodeficiency virus type 1 and simian immunodeficiency virus (89). However, a subsequent cryoelectron tomography study did not detect ordered packing of Moloney murine leukemia virus Env (28). In retrovirus particles, Env distribution may be constrained by interaction with underlying hexagonal lattices of Gag that have been observed for several retroviruses (5, 32, 33, 41, 50, 60, 90). Cryo-EM and image analysis of arenavirus particles revealed ribonucleoprotein densities that appeared to be organized in a two-dimensional, membrane-proximal lattice (62). Radial density profiles of influenza A virus particles showed that the protein density is highest in the membrane-proximal region, perhaps indicative of ordered packing (31). Freeze-fractured Sendai virus images showed that the viral matrix protein, which promotes viral assembly, is organized in two-dimensional orthogonal arrays at the fracture face of the budding membrane (1). Identical lattices of M protein have also been observed at the fracture face of the newly formed Sendai virus particles (1).

Previous reports have noted that surface protein lattices on enveloped virions become disordered with increasing time and temperature. For instance, lattices of Sendai M protein disappeared upon prolonged storage at 37°C (1), while deterioration of vaccinia virus core envelope lattices occurred more slowly during cold storage (22). The kinetics of coronavirus lattice disruption and effects on infectivity are unknown and will require further study. Nevertheless, it appears that viral assembly is guided by transient lattice formation, followed by thermal disruption of the lattice, rather than a model of nonspecific protein packing induced by low temperature. Rapid preparation, low-temperature storage, and formaldehyde fixation may have contributed to the preservation of paracrystalline lattices observed in coronavirus particles.

The lattices observed on viral particles are therefore best interpreted as remnants of the viral assembly process. Infectious coronavirus particles are assembled upon the arrival of the RNP to the pre-Golgi membranes. Although S proteins of some coronaviruses are cleaved after budding, cleavage is not required per se for infectivity (3), and S proteins of several coronaviruses, including SARS-CoV, are predominantly uncleaved (72, 87). Since coronaviruses assemble at pre-Golgi

membranes, glycans on the exposed spike ectodomains undergo additional trimming and modification. The glycosylation inhibitor TUN and inhibitors of glucosidase I and II reduce coronavirus infectivity, although inhibition of Golgi-resident mannosidases does not (66). These results are consistent with observations from other pleomorphic viruses, in which addition of high-mannose chains and initial glucosidase activity are more important than later mannosidase activity in determining infectivity (57, 84). The cores of murine and porcine coronavirus particles undergo an internal condensation in the *trans*-Golgi that does not coincide with known physical alterations to viral proteins, but they may augment infectivity (40, 70). Analysis of the cryo-EM images did not reveal any internal features within the ~25-nm-thick RNP zone proximal to the envelope. This suggests that inner core densities of mature coronaviruses are not consistently ordered with respect to the membrane. Coronavirus particles appear to bud from discrete patches of RNP subjacent to the intermediate compartment membrane (56). Results presented in this study suggest that structural protein lattice formation is integral to coronavirus budding. As a prerequisite to defining the assembly mechanism of pleomorphic coronavirus particles, it will be essential to come to an understanding of the assembly pathway that guides lattice formation.

ACKNOWLEDGMENTS

We thank Kelly Dryden and Alice Kim for technical assistance as well as Renaud Burrer and Stephen J. Crocker for helpful comments.

This work was supported by NIH grants AI-25913 (M.J.B.), AI-43103 (M.J.B.), NS-41219 (B.W.N.), AI-07354 (B.D.A.), GM-066087 (M.Y.), AI-065359 (Pacific-Southwest Regional Center of Excellence), and NIH/NIAID contract HHSN266200400058C (P.K.). During part of this work, M.Y. was also supported by a Clinical Scientist Award in Translational Research from the Burroughs Wellcome Fund. Some of the work presented here was conducted at the National Resource for Automated Molecular Microscopy, which is supported by the National Institutes of Health through the National Center for Research Resources' P41 program (RR17573).

REFERENCES

1. **Bächi, T.** 1980. Intramembrane structural differentiation in Sendai virus maturation. Virology **106:**41–49.
2. **Beards, G. M., D. W. Brown, J. Green, and T. H. Flewett.** 1986. Preliminary characterisation of torovirus-like particles of humans: comparison with Berne virus of horses and Breda virus of calves. J. Med. Virol. **20:**67–78.
3. **Bos, E. C., W. Luytjes, and W. J. Spaan.** 1997. The function of the spike protein of mouse hepatitis virus strain A59 can be studied on virus-like particles: cleavage is not required for infectivity. J. Virol. **71:**9427–9433.
4. **Bosch, B. J., R. van der Zee, C. A. de Haan, and P. J. Rottier.** 2003. The coronavirus spike protein is a class I virus fusion protein: structural and functional characterization of the fusion core complex. J. Virol. **77:**8801–8811.
5. **Campbell, S., and V. M. Vogt.** 1995. Self-assembly in vitro of purified CA-NC proteins from Rous sarcoma virus and human immunodeficiency virus type 1. J. Virol. **69:**6487–6497.
6. **Cavanagh, D.** 1983. Coronavirus IBV: further evidence that the surface projections are associated with two glycopolypeptides. J. Gen. Virol. **64:**1787–1791.
7. **Cavanagh, D.** 1983. Coronavirus IBV: structural characterization of the spike protein. J. Gen. Virol. **64:**2577–2583.
8. **Chang, C. K., S. C. Sue, T. H. Yu, C. M. Hsieh, C. K. Tsai, Y. C. Chiang, S. J. Lee, H. H. Hsiao, W. J. Wu, C. F. Chang, and T. H. Huang.** 2005. The dimer interface of the SARS coronavirus nucleocapsid protein adapts a porcine respiratory and reproductive syndrome virus-like structure. FEBS Lett. **579:**5663–5668.
9. **Conway, J. F., and A. C. Steven.** 1999. Methods for reconstructing density maps of "single" particles from cryoelectron micrographs to subnanometer resolution. J. Struct. Biol. **128:**106–118.
10. **Conway, J. F., B. L. Trus, F. P. Booy, W. W. Newcomb, J. C. Brown, and A. C. Steven.** 1993. The effects of radiation damage on the structure of frozen hydrated HSV-1 capsids. J. Struct. Biol. **111:**222–233.
11. **Corse, E., and C. E. Machamer.** 2003. The cytoplasmic tails of infectious bronchitis virus E and M proteins mediate their interaction. Virology **312:**25–34.
12. **Cowley, J. A., C. M. Dimmock, K. M. Spann, and P. J. Walker.** 2000. Gill-associated virus of Penaeus monodon prawns: an invertebrate virus with ORF1a and ORF1b genes related to arteri- and coronaviruses. J. Gen. Virol. **81:**1473–1484.
13. **Cyrklaff, M., C. Risco, J. J. Fernández, M. V. Jiménez, M. Estéban, W. Baumeister, and J. L. Carrascosa.** 2005. Cryo-electron tomography of vaccinia virus. Proc. Natl. Acad. Sci. USA **102:**2772–2777.
14. **David-Ferreira, J. F., and R. A. Manaker.** 1965. An electron microscope study of the development of a mouse hepatitis virus in tissue culture cells. J. Cell Biol. **24:**57–78.
15. **Davies, H. A., R. R. Dourmashkin, and M. R. Macnaughton.** 1981. Ribonucleoprotein of avian infectious bronchitis virus. J. Gen. Virol. **53:**67–74.
16. **Davies, H. A., and M. R. Macnaughton.** 1979. Comparison of the morphology of three coronaviruses. Arch. Virol. **59:**25–33.
17. **de Haan, C. A., M. Smeets, F. Vernooij, H. Vennema, and P. J. Rottier.** 1999. Mapping of the coronavirus membrane protein domains involved in interaction with the spike protein. J. Virol. **73:**7441–7452.
18. **de Haan, C. A., H. Vennema, and P. J. Rottier.** 2000. Assembly of the coronavirus envelope: homotypic interactions between the M proteins. J. Virol. **74:**4967–4978.
19. **De Rosier, D. J., and P. B. Moore.** 1970. Reconstruction of three-dimensional images from electron micrographs of structures with helical symmetry. J. Mol. Biol. **52:**355–369.
20. **Dryden, K. A., S. F. Wieland, C. Whitten-Bauer, J. L. Gerin, F. V. Chisari, and M. Yeager.** 2006. Native hepatitis B virions and capsids visualized by electron cryomicroscopy. Mol. Cell **22:**843–850.
21. **Dubochet, J., M. Adrian, J. J. Chang, J. C. Homo, J. Lepault, A. W. McDowall, and P. Schultz.** 1988. Cryo-electron microscopy of vitrified specimens. Q. Rev. Biophys. **21:**129–228.
22. **Dubochet, J., M. Adrian, K. Richter, J. Garces, and R. Wittek.** 1994. Structure of intracellular mature vaccinia virus observed by cryoelectron microscopy. J. Virol. **68:**1935–1941.
23. **Dubois-Dalcq, M., K. V. Holmes, and B. Rentier.** 1984. Assembly of *Coronaviridae*, p. 100–119. *In* D. W. Kingsbury (ed.), Assembly of enveloped RNA viruses. Springer-Verlag, New York, N.Y.
24. **Duquerroy, S., A. Vigouroux, P. J. Rottier, F. A. Rey, and B. J. Bosch.** 2005. Central ions and lateral asparagine/glutamine zippers stabilize the post-fusion hairpin conformation of the SARS coronavirus spike glycoprotein. Virology **335:**276–285.
25. **Escors, D., E. Camafeita, J. Ortego, H. Laude, and L. Enjuanes.** 2001. Organization of two transmissible gastroenteritis coronavirus membrane protein topologies within the virion and core. J. Virol. **75:**12228–12240.
26. **Escors, D., J. Ortego, H. Laude, and L. Enjuanes.** 2001. The membrane M protein carboxy terminus binds to transmissible gastroenteritis coronavirus core and contributes to core stability. J. Virol. **75:**1312–1324.
27. **Fischer, F., C. F. Stegen, P. S. Masters, and W. A. Samsonoff.** 1998. Analysis of constructed E gene mutants of mouse hepatitis virus confirms a pivotal role for E protein in coronavirus assembly. J. Virol. **72:**7885–7894.
28. **Förster, F., O. Medalia, N. Zauberman, W. Baumeister, and D. Fass.** 2005. Retrovirus envelope protein complex structure in situ studied by cryo-electron tomography. Proc. Natl. Acad. Sci. USA **102:**4729–4734.
29. **Frank, J.** 1990. Classification of macromolecular assemblies studied as 'single particles. ' Q. Rev. Biophys. **23:**281–329.
30. **Frank, J., B. Shimkin, and H. Dowse.** 1981. SPIDER – a modular software system for electron image processing. Ultramicroscopy **6:**343–358.
31. **Fujiyoshi, Y., N. P. Kume, K. Sakata, and S. B. Sato.** 1994. Fine structure of influenza A virus observed by electron cryo-microscopy. EMBO J. **13:**318–326.
32. **Fuller, S. D., T. Wilk, B. E. Gowen, H. G. Krausslich, and V. M. Vogt.** 1997. Cryo-electron microscopy reveals ordered domains in the immature HIV-1 particle. Curr. Biol. **7:**729–738.
33. **Ganser, B. K., A. Cheng, W. I. Sundquist, and M. Yeager.** 2003. Three-dimensional structure of the M-MuLV CA protein on a lipid monolayer: a general model for retroviral capsid assembly. EMBO J. **22:**2886–2892.
34. **Godeke, G. J., C. A. de Haan, J. W. Rossen, H. Vennema, and P. J. Rottier.** 2000. Assembly of spikes into coronavirus particles is mediated by the carboxy-terminal domain of the spike protein. J. Virol. **74:**1566–1571.
35. **Godet, M., R. L'Haridon, J. F. Vautherot, and H. Laude.** 1992. TGEV corona virus ORF4 encodes a membrane protein that is incorporated into virions. Virology **188:**666–675.
36. **Harpaz, Y., M. Gerstein, and C. Chothia.** 1994. Volume changes on protein folding. Structure **2:**641–649.
37. **He, R., F. Dobie, M. Ballantine, A. Leeson, Y. Li, N. Bastien, T. Cutts, A. Andonov, J. Cao, T. F. Booth, F. A. Plummer, S. Tyler, L. Baker, and X. Li.** 2004. Analysis of multimerization of the SARS coronavirus nucleocapsid protein. Biochem. Biophys. Res. Commun. **316:**476–483.
38. **Ho, Y., P. H. Lin, C. Y. Liu, S. P. Lee, and Y. C. Chao.** 2004. Assembly of human severe acute respiratory syndrome coronavirus-like particles. Biochem. Biophys. Res. Commun. **318:**833–838.

39. **Hoet, A. E., and L. J. Saif.** 2004. Bovine torovirus (Breda virus) revisited. Anim. Health Res. Rev. **5:**157–171.
40. **Holmes, K. V., M. F. Frana, S. G. Robbins, and L. S. Sturman.** 1984. Coronavirus maturation. Adv. Exp. Med. Biol. **173:**37–52.
41. **Kingston, R. L., T. Fitzon-Ostendorp, E. Z. Eisenmesser, G. W. Schatz, V. M. Vogt, C. B. Post, and M. G. Rossmann.** 2000. Structure and self-association of the Rous sarcoma virus capsid protein. Struct. Fold Des. **8:**617–628.
42. **Krijnse-Locker, J., M. Ericsson, P. J. Rottier, and G. Griffiths.** 1994. Characterization of the budding compartment of mouse hepatitis virus: evidence that transport from the RER to the Golgi complex requires only one vesicular transport step. J. Cell Biol. **124:**55–70.
43. **Kuo, L., and P. S. Masters.** 2002. Genetic evidence for a structural interaction between the carboxy termini of the membrane and nucleocapsid proteins of mouse hepatitis virus. J. Virol. **76:**4987–4999.
44. **Kuo, L., and P. S. Masters.** 2003. The small envelope protein E is not essential for murine coronavirus replication. J. Virol. **77:**4597–4608.
45. **Lai, M. M., and D. Cavanagh.** 1997. The molecular biology of coronaviruses. Adv. Virus Res. **48:**1–100.
46. **Lane, T. E., and M. J. Buchmeier.** 1997. Murine coronavirus infection: a paradigm for virus-induced demyelinating disease. Trends Microbiol. **5:**9–14.
47. **Lee, K. K., and J. E. Johnson.** 2003. Complementary approaches to structure determination of icosahedral viruses. Curr. Opin. Struct. Biol. **13:**558–569.
48. **Lewicki, D. N., and T. M. Gallagher.** 2002. Quaternary structure of coronavirus spikes in complex with carcinoembryonic antigen-related cell adhesion molecule cellular receptors. J. Biol. Chem. **277:**19727–19734.
49. **Li, F. Q., H. Xiao, J. P. Tam, and D. X. Liu.** 2005. Sumoylation of the nucleocapsid protein of severe acute respiratory syndrome coronavirus. FEBS Lett. **579:**2387–2396.
50. **Li, S., C. P. Hill, W. I. Sundquist, and J. T. Finch.** 2000. Image reconstructions of helical assemblies of the HIV-1 CA protein. Nature **407:**409–413.
51. **Liao, Y., Q. Yuan, J. Torres, J. P. Tam, and D. X. Liu.** 2006. Biochemical and functional characterization of the membrane association and membrane permeabilizing activity of the severe acute respiratory syndrome coronavirus envelope protein. Virology **349:**264–275.
52. **Lin, S., C. K. Lee, S. Y. Lee, C. L. Kao, C. W. Lin, A. B. Wang, S. M. Hsu, and L. S. Huang.** 2005. Surface ultrastructure of SARS coronavirus revealed by atomic force microscopy. Cell Microbiol. **7:**1763–1770.
53. **Ludtke, S. J., P. R. Baldwin, and W. Chiu.** 1999. EMAN: Semiautomated software for high-resolution single-particle reconstructions. J. Struct. Biol. **128:**82–97.
54. **Macnaughton, M. R., and H. A. Davies.** 1987. Coronaviridae, p. 173–183. *In* M. V. Nermut and A. C. Steven (ed.), Animal virus structure, vol. 3. Elsevier, New York, N.Y.
55. **Macnaughton, M. R., H. A. Davies, and M. V. Nermut.** 1978. Ribonucleoprotein-like structures from coronavirus particles. J. Gen. Virol. **39:**545–549.
56. **Massalski, A., M. Coulter-Mackie, R. L. Knobler, M. J. Buchmeier, and S. Dales.** 1982. In vivo and in vitro models of demyelinating diseases. V. Comparison of the assembly of mouse hepatitis virus, strain JHM, in two murine cell lines. Intervirology **18:**135–146.
57. **Montefiori, D. C., W. E. Robinson, Jr., and W. M. Mitchell.** 1988. Role of protein N-glycosylation in pathogenesis of human immunodeficiency virus type 1. Proc. Natl. Acad. Sci. USA **85:**9248–9252.
58. **Nagle, J. F., and S. Tristram-Nagle.** 2000. Structure of lipid bilayers. Biochim. Biophys. Acta **1469:**159–195.
59. **Narayanan, K., A. Maeda, J. Maeda, and S. Makino.** 2000. Characterization of the coronavirus M protein and nucleocapsid interaction in infected cells. J. Virol. **74:**8127–8134.
60. **Nermut, M. V., P. Bron, D. Thomas, M. Rumlova, T. Ruml, and E. Hunter.** 2002. Molecular organization of Mason-Pfizer monkey virus capsids assembled from Gag polyprotein in *Escherichia coli*. J. Virol. **76:**4321–4330.
61. **Nermut, M. V., C. Grief, S. Hashmi, and D. J. Hockley.** 1993. Further evidence of icosahedral symmetry in human and simian immunodeficiency virus. AIDS Res. Hum. Retrovir. **9:**929–938.
62. **Neuman, B. W., B. D. Adair, J. W. Burns, R. A. Milligan, M. J. Buchmeier, and M. Yeager.** 2005. Complementarity in the supramolecular design of arenaviruses and retroviruses revealed by electron cryomicroscopy and image analysis. J. Virol. **79:**3822–3830.
63. **Neuman, B. W., D. A. Stein, A. D. Kroeker, M. J. Churchill, A. M. Kim, P. Kuhn, P. Dawson, H. M. Moulton, R. K. Bestwick, P. L. Iversen, and M. J. Buchmeier.** 2005. Inhibition, escape, and attenuated growth of severe acute respiratory syndrome coronavirus treated with antisense morpholino oligomers. J. Virol. **79:**9665–9676.
64. **Ng, M. L., J. W. Lee, M. L. Leong, A. E. Ling, H. C. Tan, and E. E. Ooi.** 2004. Topographic changes in SARS coronavirus-infected cells at late stages of infection. Emerg. Infect. Dis. **10:**1907–1914.
65. **Raamsman, M. J., J. K. Locker, A. de Hooge, A. A. de Vries, G. Griffiths, H. Vennema, and P. J. Rottier.** 2000. Characterization of the coronavirus mouse hepatitis virus strain A59 small membrane protein E. J. Virol. **74:**2333–2342.
66. **Repp, R., T. Tamura, C. B. Boschek, H. Wege, R. T. Schwarz, and H. Niemann.** 1985. The effects of processing inhibitors of N-linked oligosaccharides on the intracellular migration of glycoprotein E2 of mouse hepatitis virus and the maturation of coronavirus particles. J. Biol. Chem. **260:**15873–15879.
67. **Risco, C., I. M. Anton, L. Enjuanes, and J. L. Carrascosa.** 1996. The transmissible gastroenteritis coronavirus contains a spherical core shell consisting of M and N proteins. J. Virol. **70:**4773–4777.
68. **Rossen, J. W., R. de Beer, G. J. Godeke, M. J. Raamsman, M. C. Horzinek, H. Vennema, and P. J. Rottier.** 1998. The viral spike protein is not involved in the polarized sorting of coronaviruses in epithelial cells. J. Virol. **72:**497–503.
69. **Rottier, P. J., M. C. Horzinek, and B. A. van der Zeijst.** 1981. Viral protein synthesis in mouse hepatitis virus strain A59-infected cells: effect of tunicamycin. J. Virol. **40:**350–357.
70. **Salanueva, I. J., J. L. Carrascosa, and C. Risco.** 1999. Structural maturation of the transmissible gastroenteritis coronavirus. J. Virol. **73:**7952–7964.
71. **Saxton, W. O., and W. Baumeister.** 1982. The correlation averaging of a regularly arranged bacterial cell envelope protein. J. Microsc. **127:**127–138.
72. **Song, H. C., M. Y. Seo, K. Stadler, B. J. Yoo, Q. L. Choo, S. R. Coates, Y. Uematsu, T. Harada, C. E. Greer, J. M. Polo, P. Pileri, M. Eickmann, R. Rappuoli, S. Abrignani, M. Houghton, and J. H. Han.** 2004. Synthesis and characterization of a native, oligomeric form of recombinant severe acute respiratory syndrome coronavirus spike glycoprotein. J. Virol. **78:**10328–10335.
73. **Sturman, L. S., and K. V. Holmes.** 1983. The molecular biology of coronaviruses. Adv. Virus Res. **28:**35–112.
74. **Sturman, L. S., K. V. Holmes, and J. Behnke.** 1980. Isolation of coronavirus envelope glycoproteins and interaction with the viral nucleocapsid. J. Virol. **33:**449–462.
75. **Suloway, C., J. Pulokas, D. Fellmann, A. Cheng, F. Guerra, J. Quispe, S. Stagg, C. S. Potter, and B. Carragher.** 2005. Automated molecular microscopy: the new Leginon system. J. Struct. Biol. **151:**41–60.
76. **Supekar, V. M., C. Bruckmann, P. Ingallinella, E. Bianchi, A. Pessi, and A. Carfi.** 2004. Structure of a proteolytically resistant core from the severe acute respiratory syndrome coronavirus S2 fusion protein. Proc. Natl. Acad. Sci. USA **101:**17958–17963.
77. **Surjit, M., B. Liu, P. Kumar, V. T. Chow, and S. K. Lal.** 2004. The nucleocapsid protein of the SARS coronavirus is capable of self-association through a C-terminal 209 amino acid interaction domain. Biochem. Biophys. Res. Commun. **317:**1030–1036.
78. **Tan, Y. J., E. Teng, S. Shen, T. H. Tan, P. Y. Goh, B. C. Fielding, E. E. Ooi, H. C. Tan, S. G. Lim, and W. Hong.** 2004. A novel severe acute respiratory syndrome coronavirus protein, U274, is transported to the cell surface and undergoes endocytosis. J. Virol. **78:**6723–6734.
79. **Tripet, B., M. W. Howard, M. Jobling, R. K. Holmes, K. V. Holmes, and R. S. Hodges.** 2004. Structural characterization of the SARS-coronavirus spike S fusion protein core. J. Biol. Chem. **279:**20836–20849.
80. **Vennema, H., G. J. Godeke, J. W. Rossen, W. F. Voorhout, M. C. Horzinek, D. J. Opstelten, and P. J. Rottier.** 1996. Nucleocapsid-independent assembly of coronavirus-like particles by co-expression of viral envelope protein genes. EMBO J. **15:**2020–2028.
81. **Wieringa, R., A. A. de Vries, J. van der Meulen, G. J. Godeke, J. J. Onderwater, H. van Tol, H. K. Koerten, A. M. Mommaas, E. J. Snijder, and P. J. Rottier.** 2004. Structural protein requirements in equine arteritis virus assembly. J. Virol. **78:**13019–13027.
82. **Wilk, T., F. de Haas, A. Wagner, T. Rutten, S. Fuller, R. M. Flügel, and M. Löchelt.** 2000. The intact retroviral Env glycoprotein of human foamy virus is a trimer. J. Virol. **74:**2885–2887.
83. **Wong, S. L., Y. Chen, C. M. Chan, C. S. Chan, P. K. Chan, Y. L. Chui, K. P. Fung, M. M. Waye, S. K. Tsui, and H. Y. Chan.** 2005. In vivo functional characterization of the SARS-coronavirus 3a protein in Drosophila. Biochem. Biophys. Res. Commun. **337:**720–729.
84. **Wright, K. E., R. C. Spiro, J. W. Burns, and M. J. Buchmeier.** 1990. Post-translational processing of the glycoproteins of lymphocytic choriomeningitis virus. Virology **177:**175–183.
85. **Xu, Y., Y. Liu, Z. Lou, L. Qin, X. Li, Z. Bai, H. Pang, P. Tien, G. F. Gao, and Z. Rao.** 2004. Structural basis for coronavirus-mediated membrane fusion. Crystal structure of mouse hepatitis virus spike protein fusion core. J. Biol. Chem. **279:**30514–30522.
86. **Xu, Y., Z. Lou, Y. Liu, H. Pang, P. Tien, G. F. Gao, and Z. Rao.** 2004. Crystal structure of severe acute respiratory syndrome coronavirus spike protein fusion core. J. Biol. Chem. **279:**49414–49419.
87. **Yao, Y. X., J. Ren, P. Heinen, M. Zambon, and I. M. Jones.** 2004. Cleavage and serum reactivity of the severe acute respiratory syndrome coronavirus spike protein. J. Infect. Dis. **190:**91–98.
88. **Yeager, M., E. M. Wilson-Kubalek, S. G. Weiner, P. O. Brown, and A. Rein.** 1998. Supramolecular organization of immature and mature murine leukemia virus revealed by electron cryo-microscopy: implications for retroviral assembly mechanisms. Proc. Natl. Acad. Sci. USA **95:**7299–7304.
89. **Zhu, P., E. Chertova, J. Bess, Jr., J. D. Lifson, L. O. Arthur, J. Liu, K. A. Taylor, and K. H. Roux.** 2003. Electron tomography analysis of envelope glycoprotein trimers on HIV and simian immunodeficiency virus virions. Proc. Natl. Acad. Sci. USA **100:**15812–15817.
90. **Zuber, G., J. McDermott, S. Karanjia, W. Zhao, M. F. Schmid, and E. Barklis.** 2000. Assembly of retrovirus capsid-nucleocapsid proteins in the presence of membranes or RNA. J. Virol. **74:**7431–7441.